
Article:
Krohn, J., Pepper, J. and Jackson, M. (2026) The influence of Field-Assisted Sintering Technology (FAST) temperature and cooling rate on the microstructural evolution in gamma-titanium aluminide alloy GE4822. Advanced Engineering Materials. e71126. ISSN: 1438-1656

https://doi.org/10.1002/adem.71126

Advanced Engineering Materials

ADVANCED ENGINEERING MATERIALS
www.aem-journal.com

RESEARCH ARTICLE OPEN ACCESS

The Influence of Field-Assisted Sintering Technology (FAST) Temperature and Cooling Rate on the Microstructural Evolution in Gamma-Titanium Aluminide Alloy GE4822

Jack Krohn | James Pepper | Martin Jackson

School of Chemical, Materials and Biological Engineering, University of Sheffield, Sheffield, UK

Correspondence: Jack Krohn (jjkrohn1@sheffield.ac.uk)

Received: 9 January 2026 | **Revised:** 7 May 2026 | **Accepted:** 20 May 2026

Keywords: cooling rates | field assisted sintering technology (FAST) | GE4822 | spark plasma sintering (SPS) | titanium aluminides | γ-lamellar microstructure

ABSTRACT

Field-Assisted Sintering Technology (FAST) has potential as a pre-processing step for forging γ-titanium aluminides, but its influence on the microstructural evolution of these intermetallics remains incompletely understood. This study investigates the effect of FAST dwell temperature and subsequent cooling rate on γ-lamellar colony size and volume fraction in γ-titanium aluminide alloy GE4822. Dwell temperatures were set between 1300 and 1400 °C, followed by controlled cooling at 0.1, 0.5, 1, 2 or 3 °C/s, with a free-cooling condition applied at each temperature. The γ-lamellar colony size and volume fraction were measured after dwell and cooling. At dwell temperatures below 1350 °C, γ-lamellar volume fractions remained low, regardless of cooling rate. Conversely, dwell temperatures of 1375 °C or higher produced consistently high volume fractions, with colony size increasing at slower cooling rates. The greatest microstructural sensitivity occurred at 1350 °C, where increasing the cooling rate from 1 to 2 °C/s reduced the γ-lamellar fraction from ~80% to ~10% and colony size from 200 μm to less than 50 μm. Substantial γ-lamellae colony volume fractions only formed when cooled through the α-transus, approximated at 1335 °C.

1 | Introduction and Aims

In the past decades, the intermetallic titanium aluminides have received increasing attention as an alloy system with strong potential in the aerospace and automotive industries due to their low density (~3.9 g/cm^3) and favourable elevated temperature properties [1].

Since its development in the 1980s, *General Electric's* GE4822 (Ti-48Al-2Cr-2Nb (at%)) alloy has become one of the most widely adopted titanium aluminide intermetallics. Its low density (~3.9 g/cm^3) and creep resistance at elevated temperatures have led to its application in LPT blades in the GEnX engine housed in the *Boeing 787 Dreamliner* [2–4]. The titanium alloy system is highly sensitive to aluminium content [5]. Work by Huang et al. [6] in the development of the GE4822 alloy found that 48 at% Al led to the greatest room temperature ductility, the most notable issue in this class of intermetallics.

The titanium aluminide equilibrium phase diagram remains a point of debate. Since Murray's widely accepted diagram in 1988 [7], improvements in experimental precision, including chemistry analysis, vacuum capabilities, and high temperature X-ray diffraction have led to numerous revisions, including the confirmation of a high-temperature single α phase [8–10].

Although significant progress has been made, the exact temperatures of the phase transformations are still contested, with variation between experimentally produced diagrams such as that published by *Schuster and Palm* [11] and the CALPHAD

mathematical model approach [12] utilising *ThermoCalc* software [13]. Figure 1 shows a reconstruction of *Schuster and Palm's* reassessment of the binary phase diagram. Looking at the red line indicating the peritectic solidification route at 48 at% aluminium, it would be expected that the microstructure would be a single γ phase at room temperature. However, the literature reports that this alloy exhibits a two-phase microstructure consisting of α_2 and γ phases. In GE4822, the addition of chromium stabilises the α phase and reduces the α transus temperature, altering the solidification path [14]. Upon cooling, the alloy chemistry enters the single α phase, then transitions through the α transus into the α + γ region, where γ laths nucleate and grow into the α matrix, forming a γ-lamellar microstructure. Upon further cooling, the α phase undergoes an ordering reaction to the α_2 phase, rather than entering the single γ phase, as would be expected from the binary phase diagram.

The uncertainty of the binary phase diagram is further complicated by the alloying additions in the GE4822 alloy, so the diagram should be used as a guide rather than an exact representation of the real-world transformations in this system.

Hot working of titanium aluminides is challenging, especially for peritectically solidifying titanium aluminides such as GE4822. As explored by Kremmer et al. [15], these alloys lack a ductile, high-temperature body-centred cubic β phase, resulting in a very narrow processing window. The strong influence of aluminium content further complicates hot working, as small compositional variations can significantly shift phase equilibria [1]. This sensitivity makes it difficult to establish a robust processing route. Solid-state processing via powder metallurgy helps overcome these issues by avoiding the elemental segregation associated with solidification.

An ideal pre-forging microstructure should be developed. Work by *Seetharaman and Semiatin* [16] concluded that a finer γ-lamellar grain size leads to a lower peak flow stress when hot working titanium aluminides, contrary to the *Hall-Petch* relationship. A refined fully γ-lamellar (RFL) microstructure has the best balance of properties for a successful forging outcome, with the ductility issues tied to fully γ-lamellar microstructures offset by the fine colony size. Another solid-state process technique, Pulse Magnetic Treatment (PMT) has been investigated by Li et al. [17–19]. to refine the microstructure. Figure 2 shows a schematic that represents the ideal RFL microstructure before forging, with labels for the γ-lamellar colonies, γ-laths and α_2 matrix.

Field-Assisted Sintering Technology (FAST) offers a highly controllable processing route that may enable tailoring of the GE4822 alloy to the ideal RFL microstructure. As summarised by

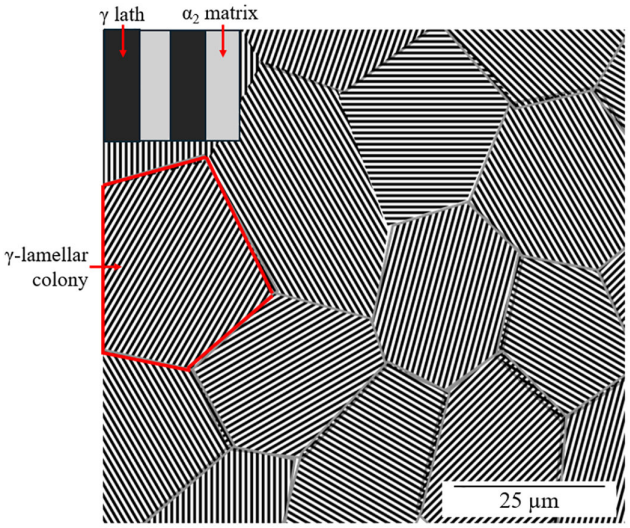

FIGURE 2 | A schematic for the ideal refined fully γ-lamellar microstructure prior to forging GE4822.

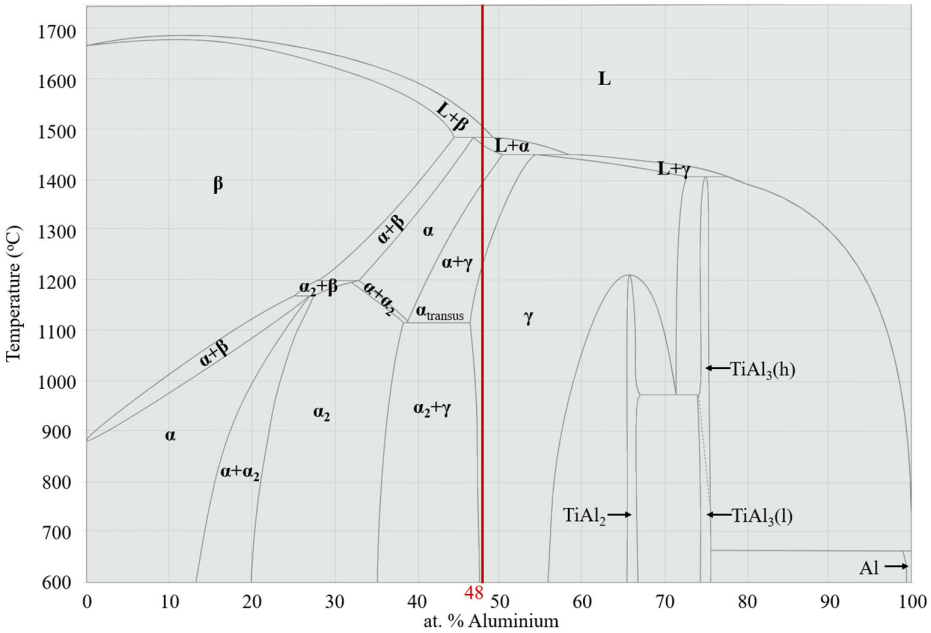

FIGURE 1 | Reconstruction of *Schuster and Palm's* reassessment of binary titanium-aluminium phase diagram, with a red line indicating the aluminium content of GE4822 alloy (after [11]).

Weston et al. [20, 21], FAST, also known as Spark Plasma Sintering (SPS), is a novel solid-state fusion technique that utilises pulsed direct current to heat the powder via the Joule heating mechanism. The high heating rates, elevated pressures, and short dwell times that can be achieved with this method make it especially suitable for materials that are traditionally difficult to sinter, such as titanium aluminides. The application of high temperatures and pressures enables full consolidation, producing a microstructure more akin to isothermal forging rather than conventional sintering.

Although some work has been performed on the effect of FAST parameters in titanium aluminides, it has primarily focused on the influence of dwell time and pressure [22]. Voisin et al. [23] attempted to obtain an RFL microstructure using FAST in a boron- and tungsten-containing titanium aluminide intermetallic termed IRIS, a β-solidifying alloy. They found that an RFL microstructure can be developed with a grain size ranging from 35 to 45 μm following a dwell in the α + β phase field. However, they suggest that grain growth is restricted by the presence of borides and a high-temperature β phase, neither of which is present in the processing of GE4822. Behrens et al. [24] found that it was possible to develop similar microstructures from varying FAST parameters. There is currently a significant gap in the literature on the influence of FAST cooling rates on titanium aluminide microstructural development. There is contention over the effect of cooling rates following heat treatments in titanium aluminides. Some sources suggest that the established microstructure types, nearly gamma, duplex, nearly γ-lamellar, and fully γ-lamellar, develop solely from holding the alloy at different regions in the single α or α + γ phase field [25]. Others find that the cooling rate influences the lath thickness in γ-lamellae, but has no apparent effect on the γ-lamellar volume fraction [26]. In contrast, *Au* [27] describes how the γ-lamellar microstructure is contingent upon the rate of cooling.

2 | Methodology

2.1 | FAST of GE4822 Powder

A parametric study was carried out to assess the microstructural influence of varying the FAST dwell temperature and subsequent cooling rate. Control of these parameters was made by altering the FAST run recipes. The dwell temperature value was input directly into each of the recipes, and the controlled cooling rates were included by specifying the target temperature and time frame to attain said temperature.

Selected FAST dwell temperatures spanned from the α + γ phase region across the α transus to the single α phase field. Previous (unpublished) FAST studies conducted on binary titanium aluminide powder (50 at% Al) had resulted in incomplete consolidation below 1275 °C. The minimum dwell temperature was selected as 1300 °C to ensure that full consolidation occurred on each run. *Schuster and Palm*'s binary phase diagram for the titanium aluminide system shows that the α transus is approximately 1400 °C for binary Ti-48Al (at%) [11]. Given the chromium additions in GE4822, it was expected that the α transus was, in fact, lower than this. Initially, 1400 °C was chosen as the upper dwell temperature limit, but would be increased if possible. While the temperature range needed to surpass the α transus, it should not exceed the liquidus temperature, which would lead to incipient melting and elemental segregation, affecting the local microstructure. A heterogeneous microstructure with macro variation in chemistry would have an unpredictable forging response. Additionally, molten material could damage the FAST machine and the graphite moulds.

Cooling rates were chosen to fully utilise the capabilities of the FAST machine. It was decided that the cooling would begin immediately following the end of the dwell period and would end once the measured temperature dropped to 600 °C. Cooling to room temperature would be uncontrolled, as the FAST machine would be unable to maintain a high cooling rate when approaching ambient temperature conditions.

A minimum linear cooling rate of 0.1 °C/s and a maximum cooling rate of 3 °C/s were selected, fully utilising the FAST machine capabilities and providing a large range of cooling conditions. Intermediate rates were chosen at 0.5, 1, and 2 °C/s. An additional uncontrolled cooling rate was included, termed *as FAST* cooling. This condition utilised the maximum cooling rates of the FAST machine from the dwell temperature to room temperature.

2.2 | Sample Preparation

The sample preparations were consistent for each FAST run. A 20 mm diameter graphite mould with matching diameter rams was selected. Graphite foil with a gauge of 350 μm was sectioned and fitted to encapsulate the internal cylindrical cavity of the graphite mould. Three 20 mm diameter graphite foil circles placed between the powder and both the upper and lower rams served to protect the graphite tooling while maintaining electrical conductivity. 12.25 g of spherical 45–150 μm GE4822 powder was weighed and poured into the graphite mould. The rams were fitted, and the powder was pre-compressed at 1 kN to increase the powder-powder contact area and improve the electrical conduction within the powder. An insulative carbon felt jacket was enclosed around the mould, with additional carbon felt rings to cover each of the rams. The parts were placed inside the *FCT Systeme GmbH Spark Plasma Sintering Furnace type HP D25* FAST machine. Additional supports were used to maintain tooling alignment and ensure temperature readings were taken from the bottom of the upper ram, as shown in Figure 3.

The powder size regularity was expected to influence the sintering and microstructural uniformity in the consolidated sample. Finer powder has a larger surface area per unit volume of powder, and hence would have favourable electrical connections and sintering rates. The *Malvern Panalytical Mastersizer 3000+ Ultra* machine was used to measure the powder size distribution (PSD) of the GE4822 powder, a graph of which is shown in Figure 4. The majority of the powder size was in the 45–150 μm range, a typical PSD for FAST. Before being poured into the graphite tooling, the powder container was shaken vigorously to ensure the powder's particle sizes remained uniformly mixed, ensuring that each FAST run used the same volume density for each size fraction.

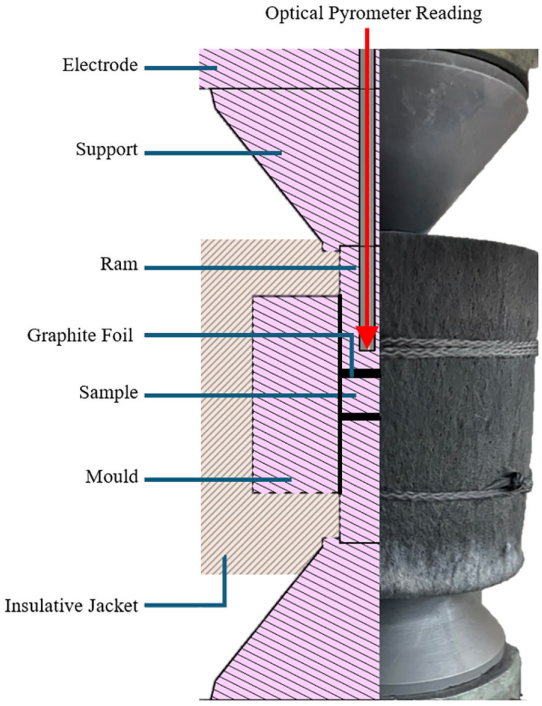

FIGURE 3 | A labelled schematic showing the setup for the FAST machine and tooling.

Besides the cooling rate and the dwell temperature, other FAST process parameters were kept consistent across the studies. A dwell time of 20 min was used in all FAST runs; it was expected that this would be sufficient for diffusional transformations to occur. The heating rate was kept constant across runs, with a rate of 50 °C/min from 450 to 1000 °C. It was then reduced to 25 °C/min until the dwell temperature was attained. The drop in heating rate served to reduce the temperature overshoot beyond the selected dwell temperature.

The FAST machine applied axial pressure gradually with increasing sample temperature, reaching a maximum of 35 MPa at 1000 °C. At this point, the titanium aluminide flow stress would be reduced, lowering the likelihood of mould breakage. Once the maximum pressure was reached, it was maintained throughout the dwell period and during cooling to 600 °C. An image detailing the temperature profile of the FAST runs with a dwell temperature of 1350 °C is shown in Figure 5. Following the FAST run, the billet was removed from the graphite mould and grit blasted to remove most of the adhered graphite foil, as shown in Figure 6.

Following the FAST runs, each consolidated sample was radially cross-sectioned and mounted in conductive Bakelite using the *Buehler Simplimet* hot mounting press. The samples were ground and polished using silicon carbide grit paper, followed by colloidal silica. Light microscopy confirmed a finish that was sufficient for scanning electron microscopy.

2.3 | Micrograph Analysis

Secondary electron and backscattered electron (Z-contrast) micrographs were acquired for each sample at both the edge and bulk regions using the *FEI Inspect F field-emission scanning electron microscope* (*FE-SEM*, *FEI Company*, *USA*). Four micrographs were obtained per sample to ensure statistically relevant analysis. Image analysis software *ImageJ* [28] was utilised to separate the α_2, γ and γ-lamellar α_2/γ colonies for morphological analysis of size and volume fraction.

Intensity thresholding enabled isolation of the α_2 phase; however, this method was ineffective in separating equiaxed γ or γ-lamellar colonies from neighbouring regions of similar contrast. As a result, manually drawn overlays on each micrograph were found to be the most accurate and repeatable method for microstructural separation, as shown in Figure 6.

The size of each grain or colony was defined by its Feret diameter, corresponding to the longest distance between two points on the perimeter. Variability in γ-lamellar colony size and volume fraction was assessed by calculating the standard deviation for each dwell temperature-cooling rate condition.

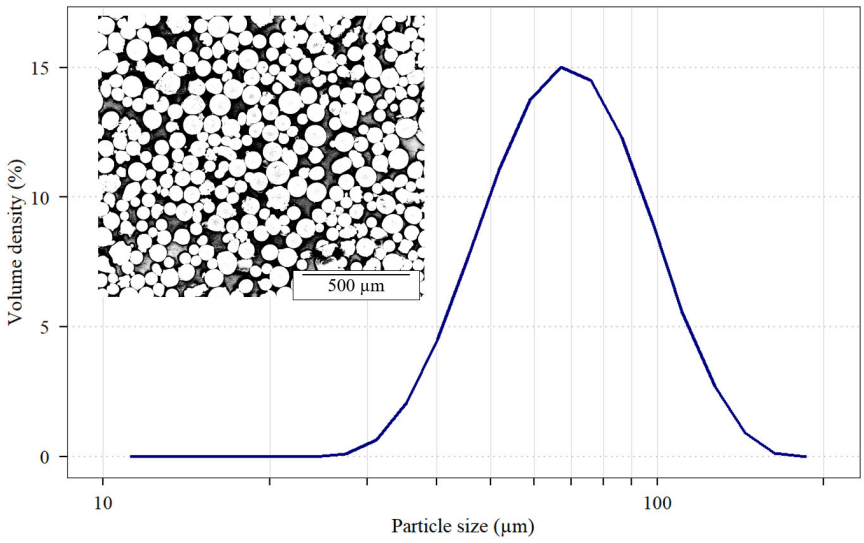

FIGURE 4 | A graph of the powder size distribution of the spherical GE4822 powder used for the FAST studies with a secondary electron micrograph of the powder.

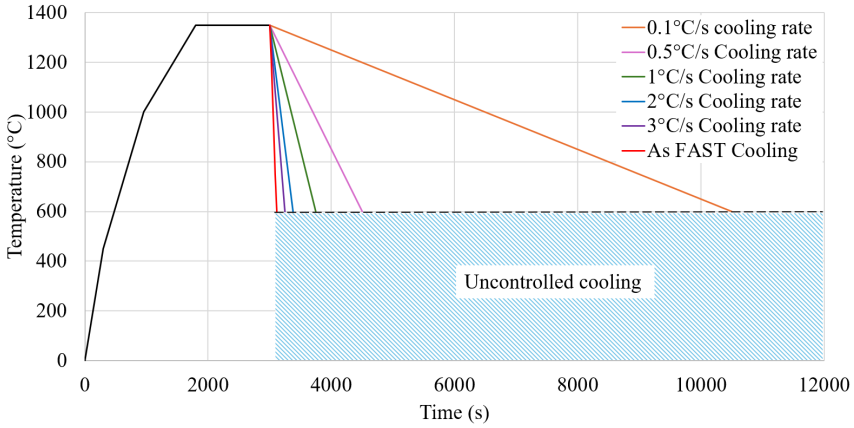

FIGURE 5 | FAST temperature profile for 1350 °C dwell temperature condition showing studied cooling rates.

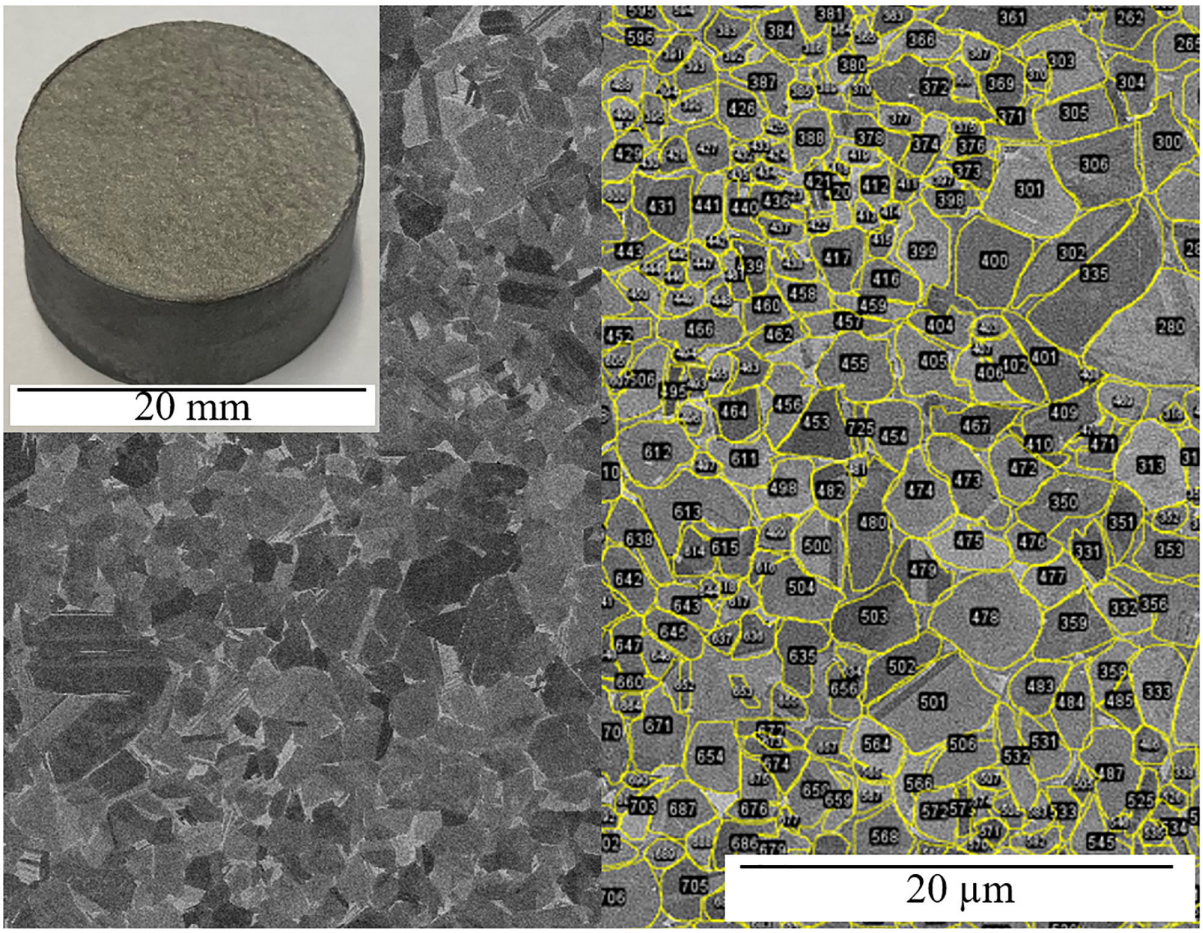

FIGURE 6 | An image exemplifying the *ImageJ* selection of equiaxed γ grains by manually outlining the grain boundaries as an overlay on top of a backscattered electron Z-contrast micrograph, with a photograph of one of the GE4822 FAST-produced billets following removal from the mould.

2.4 | Hardness Analysis

Each sample's hardness was tested using the *Mitutoyo Vickers Hardness indenter*. A hold time of 15 s was applied, as per the Vickers microhardness ASTM standard E384 [29]. A force of 1 kgF was found to be sufficient to produce a large enough indent for ease of measuring, while still allowing a sufficient indent separation (greater than three times the Feret diameter). Six sample indentations were taken with spacing conforming to the ASTM standard. Each indent corner-to-corner length was measured in µm, and the corresponding Vickers hardness value was calculated using Equation (1):

$$HV = \frac{1.854 \times F}{d^2} \tag{1}$$

where F is the applied load in kgF, and d is the diagonal length of the indent in µm [29].

2.5 | Modelling the FAST Run

Multi-physics simulation software *COMSOL 5.6* [30] was utilised to model the dwell and controlled cooling period of the FAST run. As seen in Figure 3, the optical pyrometer measured the temperature at the bottom of the upper ram rather than the sample itself, which was expected to be at a higher temperature upon completion of the dwell. A study into the temperature discrepancy between the pyrometer reading and the sample was performed to assess how closely the sample followed the prescribed thermal profile and controlled cooling rate. Additionally, the variation in temperature within the 20 mm diameter sample was evaluated to demonstrate the severity of the thermal gradient and its effect on the local cooling rate.

This study aimed to corroborate the temperature readings observed during the FAST runs, rather than provide an independent investigation into the electrical response of the PID controller during cooling. The model considered the most extreme processing condition: a dwell temperature of 1375 °C with a constant cooling rate of 3 °C/s. This condition was expected to produce the greatest discrepancy between the sample temperature and the optical pyrometer reading, as well as the steepest thermal gradient within the sample.

An axisymmetric slice of the FAST tooling and sample was modelled, including the copper electrodes, graphite mould rings, rams, foils, and supports. Cooling water was represented using a convective heat flux applied to the upper and lower electrode surfaces, with a forced convective heat transfer coefficient of 6,000 W m^{-2} K^{-1} and a constant temperature of 20 °C assumed [31]. The *Form Union* option was enabled, which modelled the bodies as remaining fixed in their position. As the purpose of this study was to model the controlled cooling period (when the powder had been consolidated), ram movement was not considered.

A piecewise function was used to input the FAST temperature profile into *COMSOL*, specifying the required temperature T as a function of time t. To model the Joule heating mechanism of FAST, the upper and lower electrodes were defined as voltage source and sink, respectively. While the FAST system regulates heating via PID control of electrical power, a simplified proportional, temperature-dependent voltage boundary condition was implemented to maintain the required temperature ramps. This simplification is justified as the model is intended to track the sample temperature when the pyrometer follows the prescribed profile, rather than to assess current variation within the FAST tooling.

An algebraic controller was utilised to vary the input voltage to the upper electrode, denoted $V_{\text{applied}}(t)$, as shown in Equation (2). If the pyrometer temperature $T_{\text{pyro}}(t)$ drops below the prescribed temperature $T_{\text{punch}}(t)$ before the end of the controlled cooling period t_6, the voltage V_{applied} is applied until the pyrometer reading exceeds the target temperature. The magnitude of the voltage response is governed by the gain parameter k_p and the temperature difference between the pyrometer reading and the prescribed value, reducing large temperature overshoots.

$$V_{\text{applied}}(t) = \begin{cases} \min\left(V_{\max},\ \max\left(0,\ k_p\left(T_{\text{punch}}(t) - T_{\text{pyro}}(t)\right)\right)\right), & t < t_6 \\ 0, & t \geq t_6 \end{cases} \tag{2}$$

The Joule heating and heat loss mechanisms were calculated using the physical partial differential equations (PDEs) contained in *COMSOL*'s multiphysics package for electrical currents (ec) and heat transfer in solids (ht). In the static form-union model, the PDE for Joule heating was simplified to Equation (3), where k is the thermal conductivity. As the FAST process is conducted in a near vacuum, additional heat losses were considered radiative only, and are defined by the radiative heat flux PDE shown in Equation (4). q_r is the heat flux per unit area, ε is the surface emissivity of the graphite tooling, taken as 0.8 from work by Maniere et al. [32], and σ_{SB} is the Stefan-Boltzmann constant.

$$\rho c_p \frac{\partial T}{\partial t} = \nabla \cdot \left(k \nabla T\right) + Q_e \tag{3}$$

$$q_r = \varepsilon \sigma_{SB}\left(T_w^4 - T_\infty^4\right) \tag{4}$$

Figure 7 shows a graphic of the COMSOL simulation of the current density distribution during the dwell period, with blue streamlines illustrating the current flow paths through the FAST tooling and titanium aluminide sample. The streamlines are overlaid on a temperature contour plot of the tooling. It can be observed that the current preferentially flowed through the graphite mould due to its higher electrical conductivity compared to the titanium aluminide sample.

A mesh convergence study was performed to find an appropriate element size and morphology to reduce computational load while maintaining the results' accuracy. It was found that a *free triangle* element type with a size *COMSOl* term *finer* was suitable.

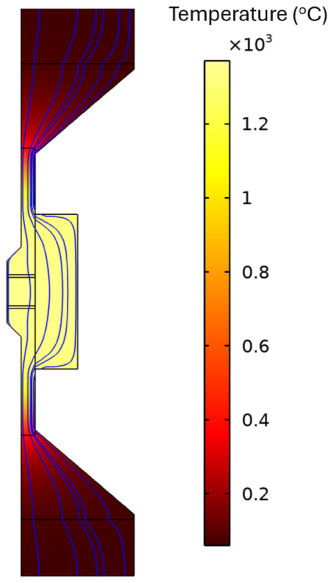

FIGURE 7 | Axisymmetric *COMSOL* simulation of the FAST tooling and sample during the dwell period. The temperature field is shown using a colour scale, and overlaid blue contour lines represent the current density distribution.

Additionally, an adaptive mesh refinement parameter was included around the region of interest to improve the accuracy of the results.

Temperature-dependent electro-thermal properties for the graphite and titanium aluminide were input into the *COMSOL* model. Egry et al. [33] investigated the thermophysical properties of high niobium-containing titanium aluminide alloy $Ti_{46.5}Al_{45.5}Nb_8$ (at%). They reported results for thermal diffusivity, electrical resistivity and specific heat capacity, from which the thermal and electrical conductivity were calculated. It was decided that Egry et al.'s data would be used for the temperature-dependent material properties in the *COMSOL* model, as the alloy chemistry investigated was similar enough to represent the GE4822 material properties satisfactorily.

Temperature-dependent material properties were also included for the Y-552 graphite components from *Olmec Advanced Materials*. The data for the electrical and thermal conductivity, specific heat capacity and surface emissivity were taken from the work performed by Pepper et al. [34], who investigated FAST microstructural control in the conventional titanium alloy Ti6Al4V.

It was decided that the temperature results would be collected from the start of the dwell period until the end of the controlled cooling period, when the average sample temperature dropped below 600 °C. Data for the heating stages before the dwell period were irrelevant and so were not collected in this study.

3 | Results and Discussion

3.1 | As Atomised Powder

Prior to the FAST study, the GE4822 'as atomised' powder was prepared for microstructural analysis. Figure 8 shows a backscattered electron Z-contrast micrograph of the powder microstructure in the as-atomised state, with some voids and cracking visible. X-ray energy dispersive spectroscopy (X-EDS) analysis was performed on three distinct regions: a lighter region, a darker interconnected region and a medium gray honeycomb region. The X-EDS results for the titanium and aluminium content in each of the regions are included. Additionally, some pockets of laths can be seen, highlighted in the red box.

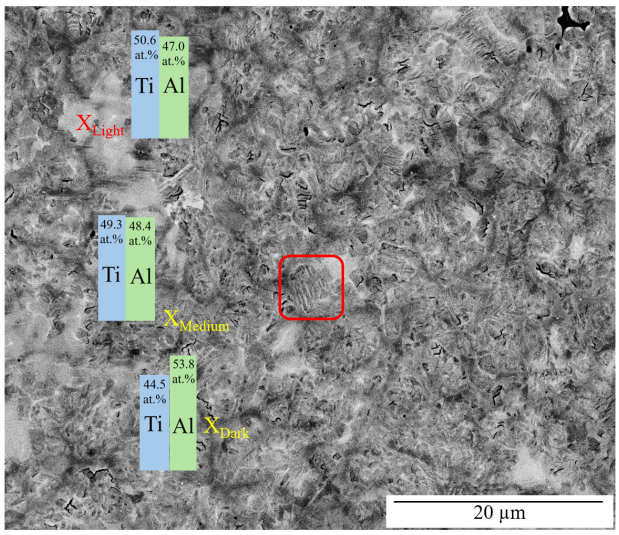

FIGURE 8 | Backscattered electron, Z-contrast micrograph of an as-atomised GE4822 powder particle, with X-EDS results included for titanium and aluminium content in 'X' locations. A red box highlights pockets of laths present in the as-atomised state.

As previously mentioned, the local aluminium content dramatically affects the solidification path in titanium aluminides, particularly around 50 at% aluminium. Figure 9 shows the region of interest in the reconstructed binary phase diagram from *Schuster and Palm* [11], with the measured X-EDS chemistries included to illustrate the solidification pathway of the dark, medium and light regions.

As the melt begins to solidify, titanium diffuses favourably into the solid, forming a titanium-rich dendrite core. The remaining aluminium-rich melt surrounds the solid phase. Upon further cooling, the melt begins to solidify, but the rate of diffusion for aluminium is too slow to allow chemical homogenisation, so the variation in aluminium content remains.

The interconnected darker regions have an Al content of around 54 at%. At this composition, solidification would have occurred through the L + α phase first. The continuous dark colouring indicates the final microstructure is a single-phase region, hence the γ phase transformed directly from the high-temperature L + α phase region.

The lighter region exhibits a phase chemistry consistent with the γ phase at room temperature; however, the high brightness in the Z-contrast image suggests it is, in fact, richer in titanium than the γ phase. Coupled with the fine equiaxed morphology, it can

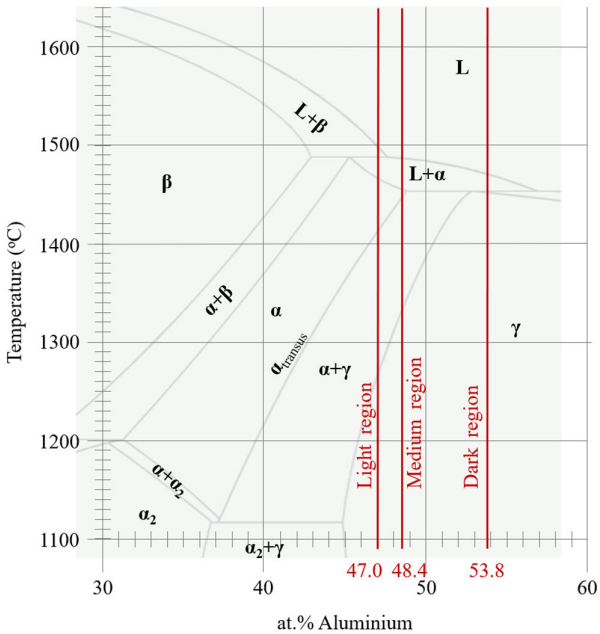

FIGURE 9 | Reconstructed binary phase diagram region of interest with aluminium contents included corresponding to the X-EDS result of the as-atomised GE4822 powder (after [11]).

be inferred that solidification for the light regions was briefly within the $L + \beta$ region, but not for long enough for dendrite formation, before transforming to the L + α and later to the single α phase, which was retained at room temperature and has a higher Z-contrast than the γ phase.

A third, medium gray microstructure, which appears somewhat honeycomb-like in morphology, can also be observed. With an average aluminium content of around 51 at%, slightly greater than in the light region, it is likely that solidification occurred through the α + L phase and then directly into the α + γ region, bypassing the single α phase.

While solidification was rapid, some γ phase had time to grow at the α grain boundaries, leading to the formation of the honeycomb morphology. Occasional pockets of laths can also be seen in this region, indicating evidence of limited γ-lamellae growth.

3.2 | Microstructural Evolution

Following the FAST runs, micrographs were taken for each dwell temperature and cooling rate condition in the bulk region of the billets. Figure 10 shows the microstructural evolution of all the dwell temperatures studied following a 1 °C/s cooling rate, except for the 1400 °C dwell condition, where only the *as FAST* uncontrolled cooling rate was studied. A clear distinction can be observed between the 1325 and 1350 °C conditions, with a dramatic increase in both γ-lamellar content and colony size.

Figure 11 details the microstructural evolution after varying the cooling rate from a 1350 °C dwell temperature. Similar to Figure 10, there is an abrupt transition between cooling rates of 1 and 2 °C, where a coarse and γ-lamellar colony-rich morphology becomes a fine near-γ microstructure.

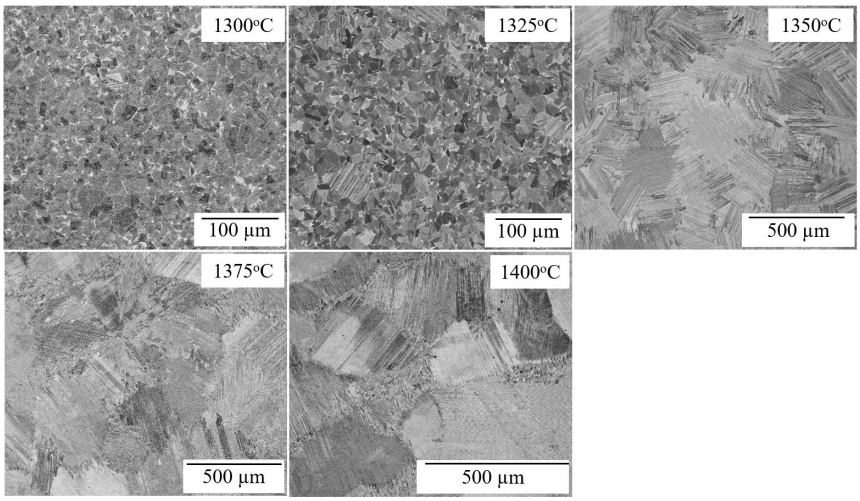

FIGURE 10 | Backscattered electron, Z-contrast micrographs of each processed billet following dwell at temperatures 1300–1400 °C and controlled cooling rate of 1 °C/s, except for the 1400 C with *as FAST* uncontrolled cooling.

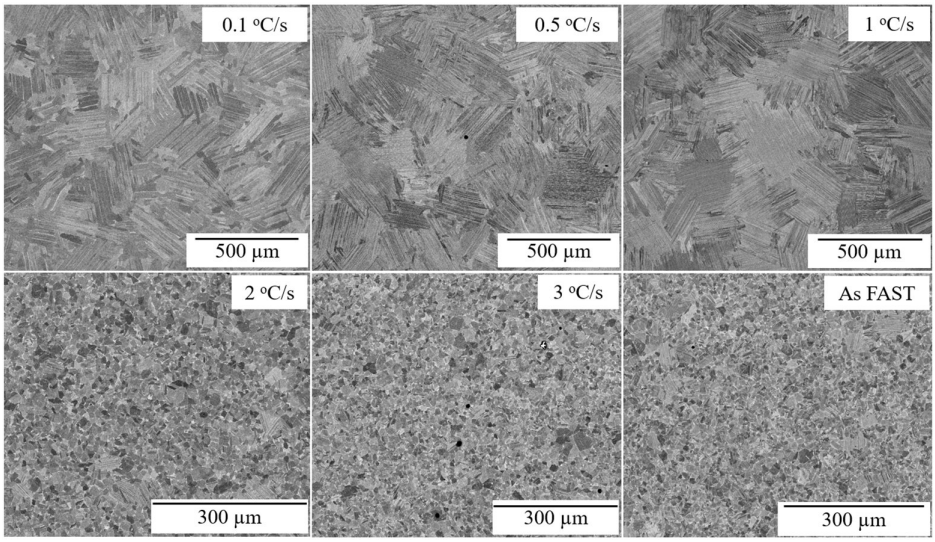

FIGURE 11 | Backscattered electron, Z-contrast micrographs of each processed billet following a 1350 °C dwell temperature and controlled cooling rates from 0.1 to 3 °C/s and uncontrolled *as FAST* cooling.

To fully investigate the variation in microstructure, the equiaxed γ grain size, γ-lamellar colony size and γ-lamellar content data were summarised using *R version 2025.05.0* [35] contour graphing tool. Black points are included to represent the data collection conditions.

Figure 12 shows a fairly consistent average γ grain size distribution of 15–20 μm across the studies. Particular coarsening can be observed at the higher dwell temperature and lower cooling rate conditions, with a maximum of just over 40 μm.

Figure 13 shows the variation in γ-lamellar colony size across the processing window. At the lower dwell temperatures of 1300–1325 °C, the lamellar colony size is consistently 50 μm or less. As the dwell temperature increases beyond 1350 °C, size is more dependent on cooling rate. This is observed most strongly in the 1–2 °C/s region with clear diagonal contour lines indicating an increase in average γ-lamellar colony size to 250 μm. At rates of 2 C/s or faster, the γ-lamellae are more resistant to growth and maintain their size of 50 μm until a higher temperature. At 1375 °C, the γ-lamellar colony size between 0.5 and 3 °C/s is 350 μm. Significant variation from this is seen at the cooling rate extremes, with 0.1 °C/s showing 600 μm and *as FAST* cooling showing just 100 μm.

Figure 14 displays a contour plot of γ-lamellar volume fraction, with three regions of interest. The lower portion shows a constant γ-lamellar volume fraction from 0% to 10%. The upper portion mirrors this, but with little variation from 80% to 90%. In between these, there is a varying transition region. Closely spaced contour lines show a rapid change in γ-lamellar fraction in this region. At 0.1 to 1 °C/s and 2 °C/s to *as FAST* cooling rates, the contour lines are near horizontal, showing cooling rate has little effect here. Closely packed and angled contours in the 1 to 2 °C/s and 1325 to 1375 °C region show that a faster cooling rate and higher dwell temperature lead to a greater γ-lamellar volume fraction between these parameters.

Line graphs of the γ-lamellar colony size and volume fraction helped to compare the microstructural response to the dwell temperature/cooling rate condition, shown in Figure 15a,b. They also helped visualise the variability in the data, with error bars showing 1 standard deviation above and below the mean value. No error bars are present for conditions that didn't yield any lamellar colonies.

The influence of cooling rate on γ-lamellar formation was found to be contingent on the dwell temperature. As seen in the contour plots, the effect of cooling rate was strongest at the 1350 °C condition.

At dwell temperatures from 1300 to 1325 °C, both γ-lamellar colony size and fraction were consistently small. Referring to Figure 16, the alloy was expected to have surpassed the γ

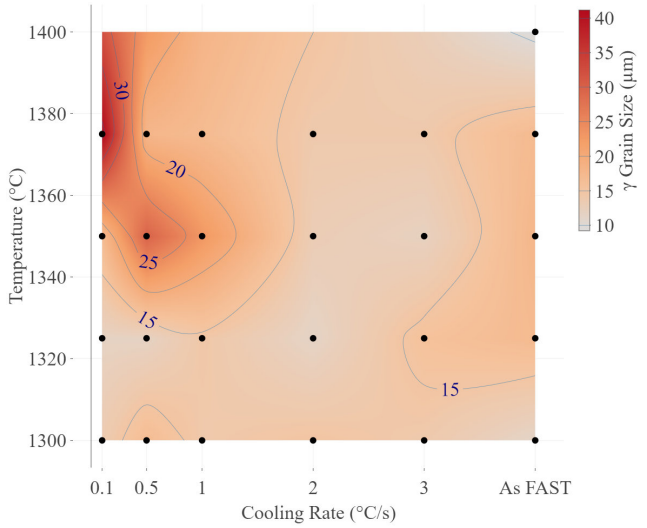

FIGURE 12 | Contour graph of variation in γ grain size (μm) following FAST processing at varying dwell temperatures (°C) and cooling rates (°C/s).

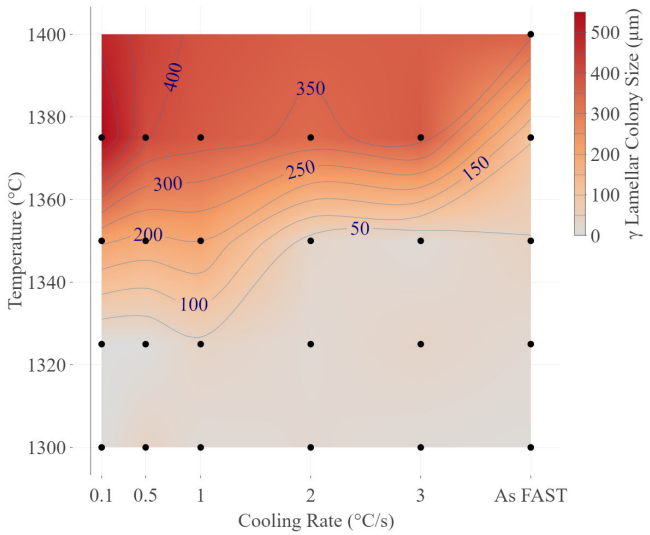

FIGURE 13 | Contour graph of variation in γ-lamellar colony size (μm) following FAST processing at varying dwell temperatures (°C) and cooling rates (°C/s).

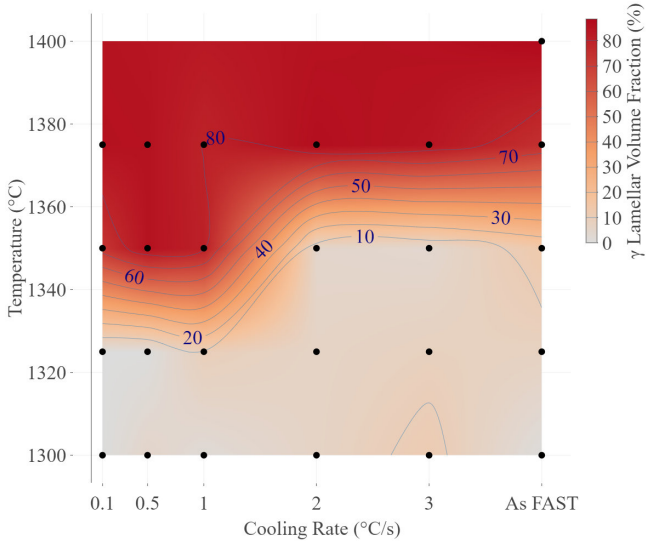

FIGURE 14 | Contour graph of variation in γ-lamellar volume fraction (%) following FAST processing at varying dwell temperatures (°C) and cooling rates (°C/s).

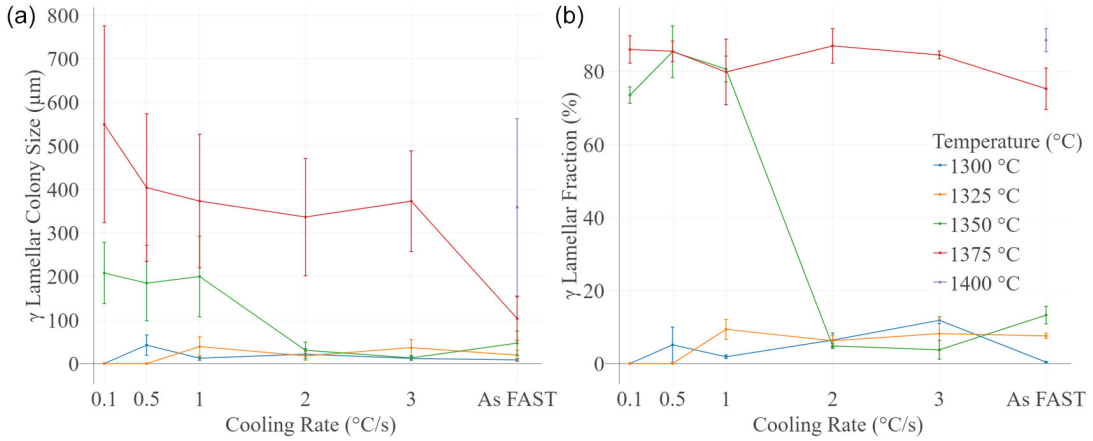

FIGURE 15 | Line graphs showing (a) the change in γ-lamellar colony size (μm) and (b) the change in γ-lamellar volume fraction (%), following FAST processing at varying dwell temperatures (°C) and cooling rates (°C/s) with error bars showing ±1 standard deviation from the mean value.

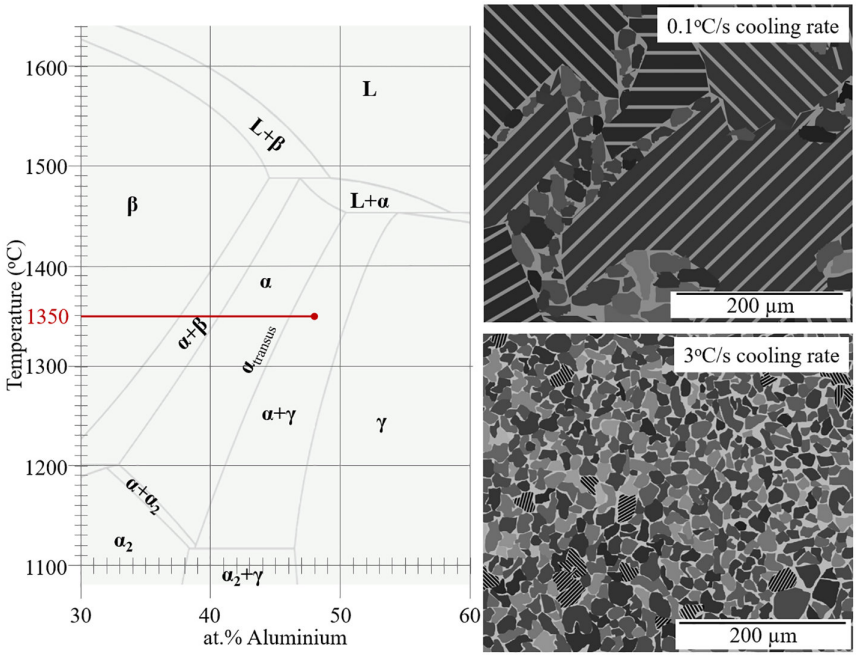

FIGURE 16 | Reconstruction of *Schuster and Palm's* reassessment of the binary titanium-aluminium phase diagram region of interest with micrograph schematics illustrating the cooling rate effect following a FAST dwell at 1350 °C (after [11]).

transition, entering the α + γ phase field. At 1325 °C, the driving force for atomic diffusion was greater than at 1300 °C, so an increase in γ-lamellar colony size was expected. Instead, the microstructures remained remarkably similar, indicating that diffusion kinetics alone did not govern γ-lamellar colony formation in this two-phase field.

At 1375 °C, the alloy had surpassed the α transus, entering the single α phase field. Irrespective of cooling rate, a high γ-lamellar content of approximately 80% was observed, in contrast to the low γ-lamellar content measured at 1300–1325 °C across all cooling rates. This indicated that γ-lamellar formation occurred only during cooling through the *α* transus. At 1375 °C, complete dissolution of the γ phase into a single α phase was achieved. Upon cooling, γ laths nucleated at α grain boundaries and grew into the retained α matrix, producing the observed high γ-lamellar content.

Greater variability was observed in the γ-lamellar colony size at 1375 °C, where, in general, increasing the cooling rate led to a decrease in Feret diameter. Having passed the α transus, no γ grains remained to pin the α grain boundaries, allowing unrestricted grain growth. At a constant temperature, the total growth of the α grains was governed by the time spent within the single α phase field. Slower cooling rates effectively increased the time in this field, rather than directly influencing the growth kinetics. The single data point obtained at 1400 °C supported this interpretation. The higher temperature accelerated grain coarsening by providing a greater driving force for atomic diffusion and by extending the period available for grain growth through the longer heating and cooling duration.

The 1350 °C condition exhibited the most pronounced sensitivity to cooling rate. At cooling rates of 1°C/s or less, the γ-lamellar fraction was similar to that observed at 1375 °C, suggesting that

the time spent in the single α phase was sufficient for complete γ dissolution. Conversely, at cooling rates of 2 °C/s or greater, the γ-lamellar fraction was comparable to that measured at 1325 °C, indicating limited γ dissolution and suppression of γ-lamellar formation. Evaluation of Figure 16 shows that, at 1350 °C and 48 at% aluminium, the alloy would be expected to lie in the α + γ region. In contrast, the observations indicate that the alloy had just surpassed the α transus. Uncertainty in the binary phase diagram, compounded by the α-stabilising effect of chromium, suggests that the actual α transus is lower than predicted from Figure 16.

The γ-lamellar colony size exhibited a similar trend at the 1350 °C condition. At cooling rates of 1 °C/s or slower, where significant γ-lamellar colonies developed, the average grain size remained around 200 μm. The consistency of the grain size indicated that the driving force for grain growth was low, and longer time spent at elevated temperature had less influence on the final γ-lamellar colony size than observed at 1375 °C.

The decrease in γ-lamellar colony size and volume fraction between 1 and 2 °C/s indicated that the cooling rate and the effective dwell time at this temperature were critical. Based on evidence that the α transus had been surpassed at this temperature, it was estimated to lie at approximately 1335 °C. Using this approximation, the period during which the billet remained above the α transus differed by only 7.5 s between the two cooling rates. Such a dramatic decrease in γ-lamellar volume fraction over this small time interval warranted further investigation.

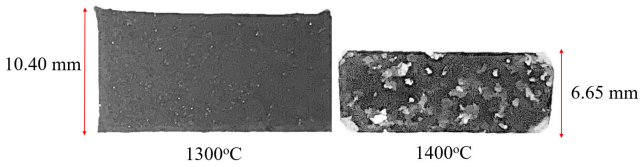

FIGURE 17 | Light macrograph of the billet cross-section, illustrating the variation in thickness due to some melting at 1400 °C.

Analysis of the FAST run temperature data revealed that the 1 °C/s run overshot to 1355 °C, compared to 1352 °C in the 2 °C/s run. The higher dwell temperature in the slower cooling run may account for the observed jump in γ-lamellar volume fraction.

As shown in Figure 15b, some γ-lamellar colonies were present following FAST at the 1300–1325 °C dwell temperatures. This was attributed to the retention of metastable α phase in the powder after atomisation. Upon heating into the α + γ phase field, these regions effectively passed through the α transus and produced the small, isolated γ-lamellar colonies that were observed.

3.3 | Processing at 1400 °C

Temperature, pressure and ram movement data were analysed following each FAST run to ensure that the correct parameters were achieved. In the first 1400 °C run with an *as FAST* cooling rate, two successive peaks in piston speed were observed. In cooler dwell temperature runs, a single piston speed peak (mm/s) occurred once the temperature and pressure were sufficient to overcome the flow stress and consolidate the powder. The second peak in the 1400 °C FAST run corresponded to gradual local melting of the material, with the molten material being forced out of the gap between the mould and the ram. Figure 17 shows the variation in puck thickness following FAST runs at 1300 and 1400 °C, highlighting the loss of material in the higher-temperature run due to melting. As discussed, FAST is a solid-state process, which avoids common microstructural features associated with melting, such as excessive grain growth, dendrite formation, and elemental segregation. To obtain a desirable RFL microstructure for a good forging response, an upper dwell temperature limit of 1375 °C is recommended. To prevent damage to the graphite tooling, no further FAST runs were conducted at 1400 °C.

3.4 | *As FAST* Cooling

The *as FAST* cooling studies explored the influence of a more rapid, non-constant cooling condition. Figure 18 shows the initial

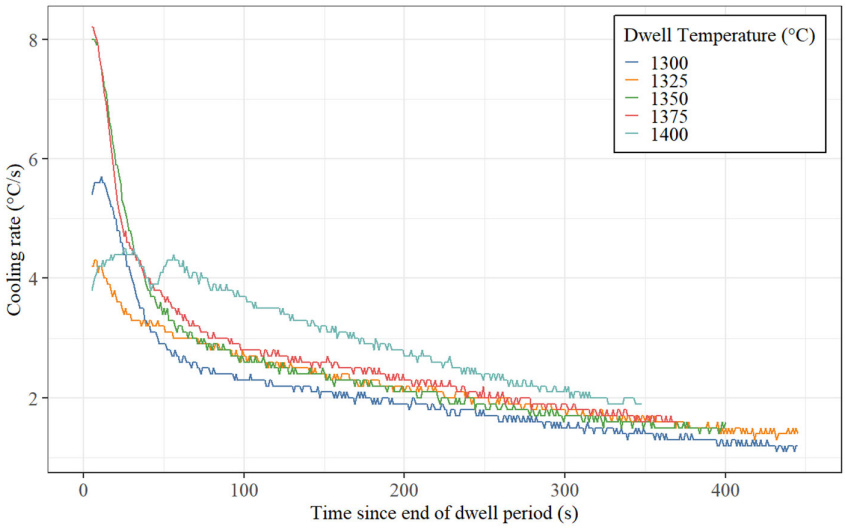

FIGURE 18 | A graph showing the variation in uncontrolled cooling rate (°C/s) from the dwell period for each studied FAST dwell temperature (°C).

cooling rate from dwell for each of the *as FAST* cooling studies, with the data cut off once the optical pyrometer temperature dropped below the minimum measurable reading of 250 °C.

It was anticipated that the initial cooling rate would increase with dwell temperature due to the greater thermal drive; however, the 1400 °C run exhibited an initial rate of only 5 °C/s. This reduced rate was likely a result of local melting at this temperature, which limited the speed of heat transfer between the sample and the tooling. The cooling rate for the 1300 C dwell condition was unexpectedly greater than for 1325 °C. This was likely due to variation in uncontrolled FAST parameters, such as the temperature of the cooling water. Additionally, the 1350 and 1375 °C conditions exhibited very similar initial cooling rates at just over 8 °C/s. There was a greater drive for heat transfer in the 1375 °C condition, yet there was barely a corresponding increase in cooling rate. At these elevated dwell temperatures, the maximum cooling rate appeared to be limited by the rate of heat transfer through the tooling.

The *as FAST* condition represents the maximum achievable cooling rate of the system. Without the FAST machine actively using Joule heating to maintain stability, the temperature distribution was sensitive to small variations, resulting in a more volatile cooling rate.

Nonetheless, the effect of uncontrolled cooling on the microstructure was minimal. Examination of Figure 15 showed that the *as FAST* cooling condition generally continued the trend established by the earlier controlled cooling rates. The only exception occurred for the γ-lamellar colony size data at 1375 °C, where a rapid decrease in size was observed from the 3 °C/s condition. This decline mirrored the change observed between 1 and 2 °C/s at 1350 °C and also represented a region of microstructural sensitivity. The faster cooling rate reduced the time spent within the single α phase field, shortening the period available for grain growth and causing the sharp drop in average γ-lamellar colony size.

3.5 | Temperature Distribution Modelling and FAST Data

A *COMSOL* multi-physics study was conducted to assess the variation between the optical pyrometer temperature reading and the average sample temperature during the FAST dwell and cooling periods. Additionally, the maximum and minimum temperatures within the sample were examined to investigate the thermal gradient during the FAST run. Data were collected for the most extreme temperature and controlled cooling condition, where the greatest temperature variation was expected, namely the 1375 °C dwell condition with a linear 3 °C/s cooling rate.

Figure 19 shows the variation in temperature between the optical pyrometer reading and the average sample temperature. During the dwell period, the pyrometer reading was consistently 1 °C lower than the average sample temperature. This was expected, as heat was lost between the sample and the upper ram. The temperature discrepancy was small and was not considered to significantly affect the microstructural evolution.

Immediately following the end of the dwell period, the discrepancy between the optical pyrometer reading and the average sample temperature spiked to the maximum observed during the study, at just over 12 °C. As heat was primarily extracted from the upper and lower electrodes through the cooling water, a thermal gradient was established. The optical pyrometer reading was located closer to the convective cooling flux than the sample and therefore cooled more rapidly. The temperature variation decreased gradually during the cooling period, falling below 6 °C by the end of the controlled cooling period.

Although the initial temperature difference is moderate, the effect on the local sample cooling rate is inconsequential. Figure 20 shows the average sample cooling rate during the controlled cooling and free cooling periods. The initial cooling rate barely

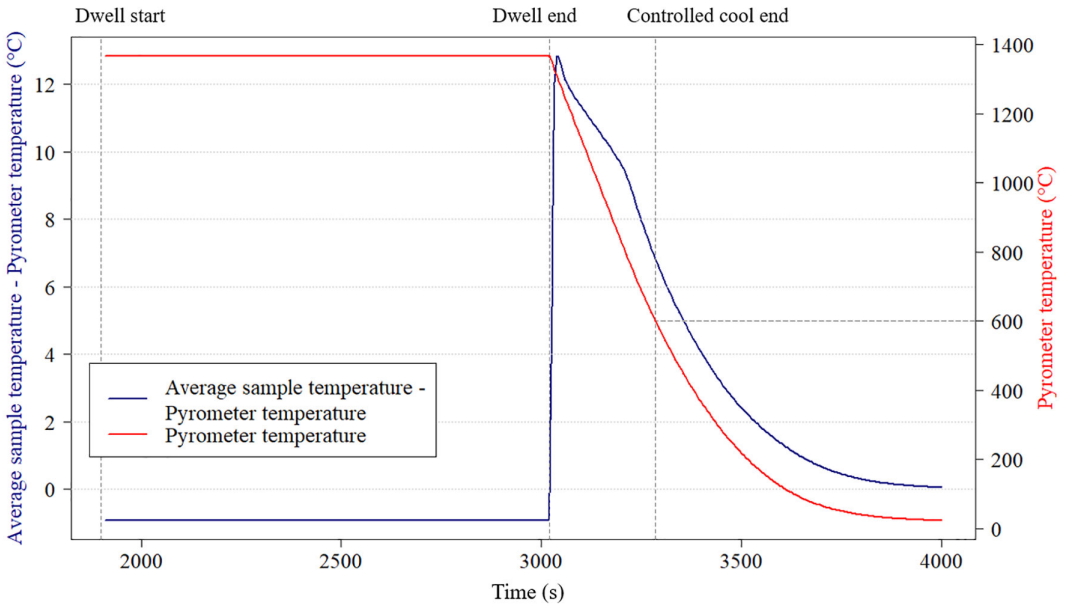

FIGURE 19 | A graph showing the *COMSOL* model results for the difference between the pyrometer temperature reading and the average titanium aluminide sample temperature during the 1375 °C dwell temperature and 3 °C/s controlled cooling FAST run.

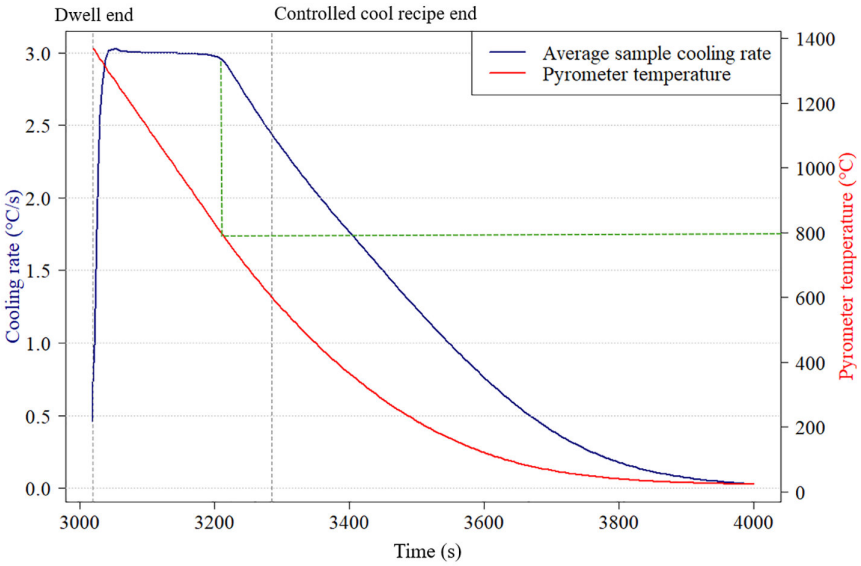

FIGURE 20 | A graph showing the *COMSOL* model results for the variation in the sample average cooling rate during the cooling stage of the 1375 °C dwell temperature and 3 °C/s controlled cooling FAST run, with green dotted lines indicating the instance and temperature when the controlled cooling rate would no longer be maintained.

exceeds 3 °C/s and is very short-lived. What can be observed is that the cooling rate drops below 3 °C/s before the end of the controlled cooling period. As the system approaches ambient temperature, the cooling water is unable to maintain the high rate of heat extraction. Instead of maintaining a controlled cool until 600 °C, it is maintained till approximately 800 °C. Looking at Figure 9, the system has cooled well below the α transus, and is comfortably in the $\alpha_2 + \gamma$ phase. A drop in cooling rate from this temperature is highly unlikely to significantly influence the microstructural development.

To verify the *COMSOL* model, the actual FAST temperature data and cooling rate were plotted for the 1375 °C dwell temperature and 3 °C/s cooling rate condition, as shown in Figure 21. In this run, the cooling rate exhibited some fluctuation, with an initial spike to 3.5 °C/s. Under this condition, strong competition between Joule heating and the imposed high cooling rate led to some instability in the thermal response.

Following this, the cooling rate settled at 3 °C/s before gradually decreasing to lower values prior to the end of the controlled cooling period. The cooling rate consistently dropped below 3 °C/s at just under 900 °C, as indicated by the horizontal dotted line in Figure 21. This behaviour closely matched the *COMSOL* simulation, providing further validation of the model's reliability.

The variation in controlled cooling rate raised concerns regarding whether the FAST machine could maintain the imposed rates at

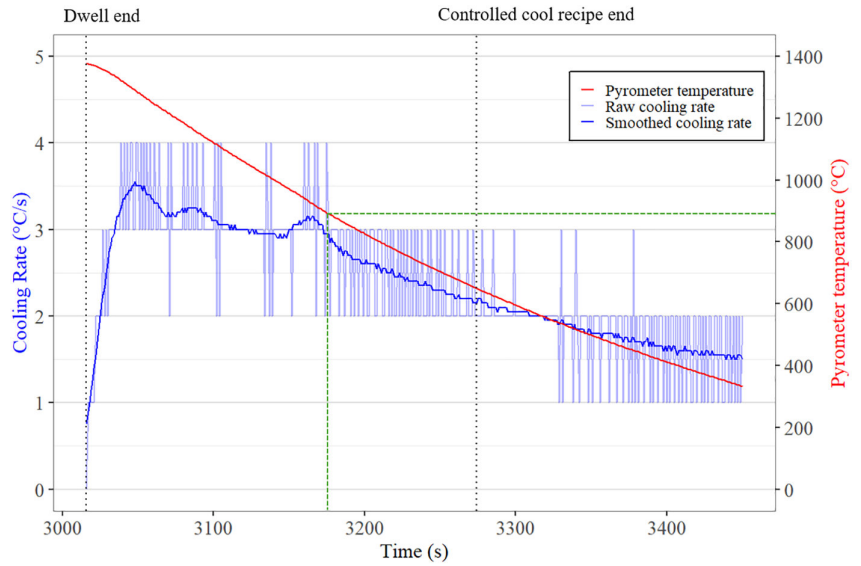

FIGURE 21 | A graph of the raw and smoothed cooling rate data for the 1375 °C dwell temperature and 3 °C/s controlled cooling rate condition, with green dotted lines indicating the instance and temperature when the controlled cooling rate could no longer be maintained.

lower values. To investigate this, the FAST run data and cooling rate were examined for the 1375 °C dwell temperature and 2 °C/s cooling rate condition, as shown in Figure 22. Far less fluctuation was observed under this condition, with the cooling rate quickly stabilising at 2 °C/s for the entire controlled cooling period. A brief increase in cooling rate occurred at the end of the controlled cooling period, as free cooling initially allowed a faster rate before decreasing as the pyrometer reading approached ambient temperature. As the FAST data confirmed that the 2 °C/s cooling rate had been maintained, it was inferred that the less extreme cooling rates were also maintained throughout the controlled cooling period. This demonstrated that the cooling rate was reliably maintained even under the most sensitive condition, the 1350 °C dwell temperature with cooling rates between 1 and 2 °C/s.

Some temperature variation was also observed within the sample. Figure 23 shows the total sample temperature variation during the FAST run. During the dwell period, a consistent temperature discrepancy of just over 3 °C was present. At the start of the controlled cooling, the variation spiked to a maximum of 9 °C before gradually diminishing. Figure 24 shows the sample temperature variation across the radial axis and along the axial axis. At the end of the dwell period, radial temperature variation dominated at almost 5 °C, as heat was lost through conduction into the graphite mould and by radiation into the FAST chamber. As cooling commenced, axial temperature variation immediately increased from less than 1 °C to almost 7 °C, as heat was extracted primarily through the upper and lower surfaces of the sample, producing a strong thermal gradient. Following completion of the

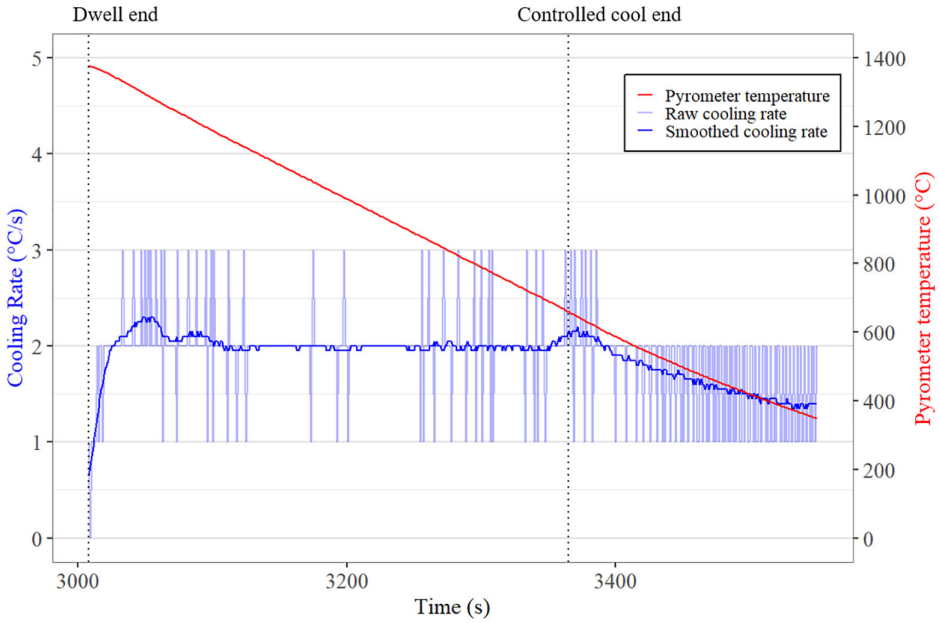

FIGURE 22 | A graph of raw and smoothed cooling rate data for the 1375 °C dwell temperature and 2 °C/s controlled cooling rate condition.

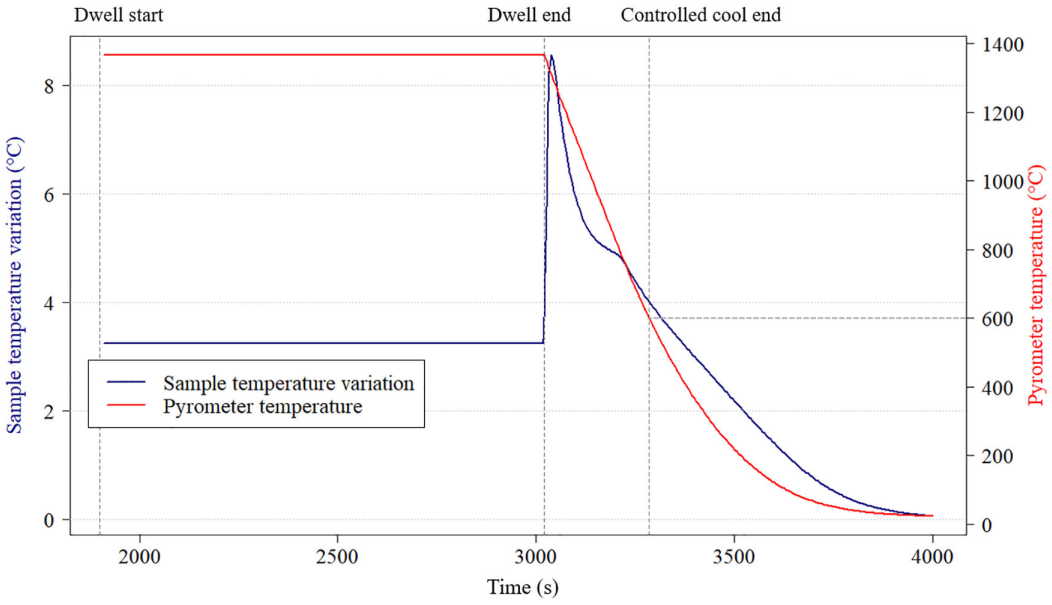

FIGURE 23 | A graph showing the *COMSOL* model results for the variation in temperature of the titanium aluminide sample during the 1375 °C dwell period and 3 °C/s controlled cooling FAST run.

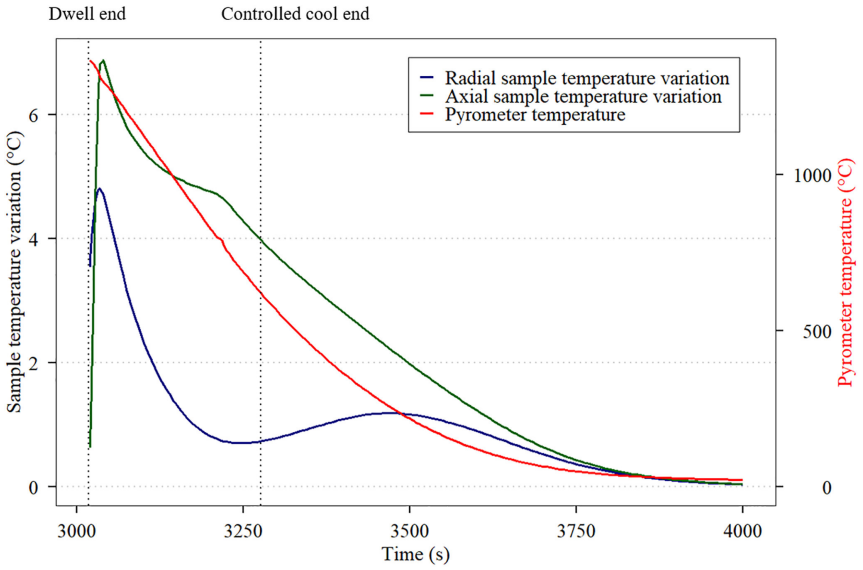

FIGURE 24 | A graph showing the *COMSOL* model results for the radial and axial variation in temperature of the titanium aluminide sample during the cooling stage of the 1375 °C dwell temperature and 3 °C/s controlled cooling FAST run.

controlled cooling, both axial and radial temperature variations approached thermal equilibrium, reducing to 0 °C.

For this 20 mm diameter sample, the small temperature variation during dwell was not expected to significantly influence microstructural evolution. However, in larger samples, it is anticipated that radial temperature variation during the dwell period and axial temperature variation during cooling would be exacerbated, potentially leading to a heterogeneous microstructure.

3.6 | Hardness Results

Hardness measurements were made across each sample. Figure 25 shows how the average hardness varies with each dwell temperature and cooling rate condition. Generally, hardness increases with cooling rate, particularly between 0.1–0.5 °C/s for dwell temperatures other than 1350 °C.

At the 1375 °C dwell temperature, the γ-lamellar colony fraction remained stable across the measured cooling rates, while the colony volume fraction decreased. This trend is most evident between 0.1 and 0.5 °C/s, mirroring the hardness data and highlighting an inverse relationship between γ-lamellar colony size and hardness.

The increase in hardness at the 1300 and 1325 °C conditions is more surprising, as there was no apparent variation in equiaxed γ or γ-lamellar colony size or fraction. Given the very low γ-lamellar content, the γ-lath thickness is also unlikely to have influenced the measured hardness, suggesting further investigation is needed to explain this variation.

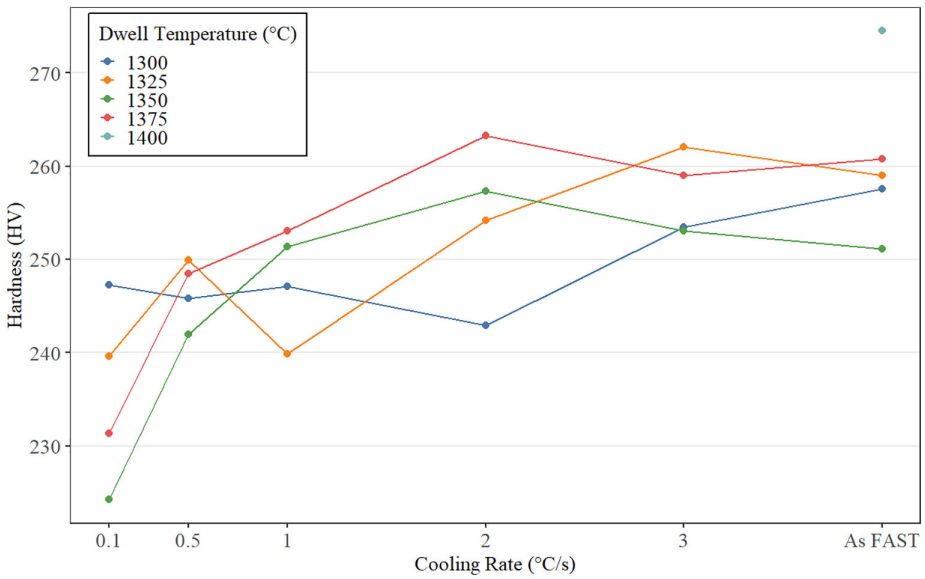

FIGURE 25 | A graph showing the variation in sample hardness (HV) with dwell temperature (°C) and cooling rate (°C/s) condition.

The highest hardness was measured for the single 1400 °C dwell temperature with *as FAST* cooling rate. This condition also exhibited the greatest γ-lamellar fraction, confirming that a fully γ-lamellar microstructure produces the highest hardness.

Somewhat unexpected results were observed at the 1350 °C condition, where the greatest microstructural sensitivity was seen. The γ-lamellar colony fraction dropped sharply from 80% at 1 °C/s to less than 10% at 2 °C/s. Literature generally reports that fully γ-lamellar microstructures have the lowest ductility, so a corresponding decrease in hardness might be expected; however, an increase from approximately 251 HV to 257 HV was observed.

Reviewing previous studies, the average hardness of titanium aluminide GE4822 is reported to be approximately 300–400 HV [36]. The lower absolute values measured here warrant further investigation. Nevertheless, the trends and correlations observed remain valid and accurately reflect the microstructural evolution and mechanical response.

3.7 | Chemical Analysis

X-Ray Fluorescence (XRF) was carried out using the *Bruker XRF S2 PUMA* machine on the GE4822 sample puck following a 1300 °C FAST run to verify the alloy chemistry. Table 1 shows the composition of the alloy following conversion to at%. While XRF results generally follow the expected Ti-48Al-2Cr-2Nb at% chemistry closely, the aluminium content is greater than expected at 49.5 at%.

To verify the unexpected XRF results, further chemical analysis was conducted at the *Sheffield Analytical Services* department in the *Sheffield Assay Office*. Chemical composition tests were performed on the expected alloying elements (titanium, aluminium, chromium, and niobium). Additional tests were carried out to quantify low atomic weight elements that XRF cannot reliably detect, namely nitrogen, oxygen, and carbon.

Several testing methods were employed. For the expected alloying elements, Inductively Coupled Plasma-Optical Emission Spectroscopy (ICP-OES, ASTM E2371-21a) was used [37]. Oxygen and nitrogen contents were measured using Inert Gas Fusion (IGF, ASTM E1409-13) [38], while carbon content was determined via combustion and infrared absorption (ASTM E1915-20) [39].

These tests were conducted on the GE4822 alloy in three states: as atomised powder, as a solid puck following a FAST dwell at 1300 °C, and as a solid puck following a FAST dwell at 1375 °C. For the solid samples, material was extracted from the bulk to avoid any surface-level carbon ingress skewing the results. Since FAST is a solid-state process conducted in vacuum, the alloy composition was expected to remain constant, and testing after the higher-temperature FAST condition verified this assumption.

Table 2 shows minimal variation between the powder and solid GE4822 compositions. This indicates that the FAST process did not significantly alter the chemistry from powder to solid form, at least for dwell temperatures up to 1375 °C. The average aluminium content remained consistently close to 46 at%, lower than both the XRF results and the expected alloy composition. According to the binary phase diagram of *Schuster and Palm* [11], this lower aluminium content results in the α transus being surpassed at a lower temperature, as observed in the 1350 °C results.

The oxygen content appeared to be affected by the FAST process. The oxygen at% increased most significantly between the 'as atomised' powder and the 1300 °C FAST condition, with a further increase observed for the 1375 °C condition. This behaviour is consistent with the expected increase in oxygen pick-up at higher temperatures, likely originating from the limited atmosphere present in the vacuum chamber.

Greater confidence can be placed in the *Assay Office* results than the XRF results, as the former employed techniques specifically developed for quantifying elemental contents in titanium alloys.

3.8 | Carbon Ingress from Graphite Tooling

Following the FAST runs, evidence of carbon ingress was observed on the outer surface of some samples, corresponding to the areas in contact with the graphite foil circles. Figure 26 shows a backscattered electron (BSE) Z-contrast micrograph with X-EDS maps, including zoomed regions of interest from the outer region of a billet following a 1350 °C dwell and 1 °C/s controlled cooling. Four distinct layers were observed from the outer surface towards

TABLE 1 | XRF elemental composition results of the GE4822 billet following FAST with 1300 °C dwell temperature, rounded to 1 d.p.

Content	Titanium	Aluminium	Chromium	Niobium	Iron
wt%	57.8	34.6	2.4	5.0	0.1
at%	46.5	49.5	1.8	2.1	0.1

TABLE 2 | Elemental composition results (at%) from the *Sheffield Assay Office* of the GE4822 alloy in the as-atomised powder state and after FAST processing at 1300 and 1375 °C, rounded to 4 significant figures.

Condition	Ti	Al	Cr	Nb	O	N	C
Powder, at%	49.62	46.10	1.824	2.116	0.2787	0.02315	0.03375
1300 °C FAST, at%	49.66	45.92	1.814	2.088	0.4049	0.03180	0.08765
1375 °C FAST, at%	49.54	46.03	1.829	2.100	0.4553	0.02889	0.01685

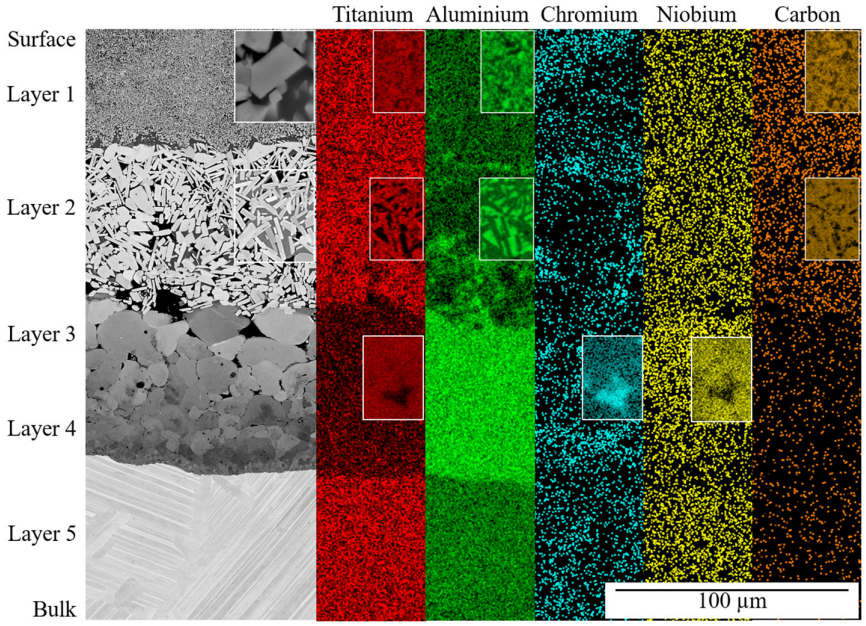

FIGURE 26 | BSE micrograph with X-EDS maps of a region showing carbon ingress, located on the outer surface of a billet following a 1350 °C dwell temperature and 1°/s controlled cooling rate.

the bulk. X-EDS point analyses and line scans were conducted to aid in identifying the phases of these layers.

The outermost layer exhibited a porous distribution of a fine, angular phase. In the zoomed regions, areas rich in titanium and carbon coincided, surrounded by an aluminium-rich matrix. Based on X-EDS point analysis, the composition of the angular fine phase was estimated, with an average titanium-to-aluminium atomic ratio of approximately 2:1 and some carbon detected. Although X-EDS has limited accuracy for low atomic number elements such as carbon, confidence in the titanium and aluminium content, combined with the presence of carbon, suggests that this phase was likely the titanium aluminide complex carbide Ti_2AlC. This phase exhibited an equiaxed yet angular morphology similar to that reported by Yang et al. [40]. and Hashimoto et al. [41].

Moving towards the bulk, the second layer exhibited a high-aspect-ratio, angular, coarse phase typical of a carbide. The X-EDS maps again showed coinciding titanium- and carbon-rich regions, with free aluminium surrounding the carbide phase. Point analysis indicated that this phase was another titanium aluminide complex carbide, Ti_3AlC.

The third and fourth layers, located just before the bulk γ-lamellar phase, exhibited distinct morphologies. Layer 3 had a coarser structure with extensive voiding, while layer 4 was finer with reduced void fraction, indicating greater consolidation. Both layers were aluminium-rich, and this was the first region in which niobium- and chromium-rich areas were no longer coincident, with higher chromium content observed in the voids. Point analyses confirmed a titanium-to-aluminium ratio of approximately 1:3. According to the reconstruction of *Schuster and Palm's* binary phase diagram [11] in Figure 1, this composition corresponds to the high-aluminium $TiAl_3$ phase. It is likely that, following carbon ingress, free aluminium diffused from the titanium aluminide carbide regions to form this aluminium-rich layer.

Finally, the transition to the bulk, fully γ-lamellar titanium aluminide morphology was observed. Well-defined boundaries and the rapid depletion of carbon into the bulk indicate that carbon ingress was limited and could be effectively removed during a subsequent machining stage.

4 | Conclusions

This study has enabled several conclusions to be drawn regarding the effect of cooling rate on FAST (Field-Assisted Sintering Technology) runs conducted at varying dwell temperatures:

1. FAST dwell temperatures below 1325 °C result in a predominantly γ-phase microstructure, largely independent of the cooling rate.
2. FAST dwell temperatures above 1375 °C lead to highly γ-lamellar microstructures, where the γ-lamellar volume fraction is also largely unaffected by cooling rate. The colony size is more heavily influenced by cooling rates, with greater rates leading to a more refined microstructure.
3. At a dwell temperature of 1350 °C, the microstructure is highly sensitive to cooling rate and dwell time, with dramatic decreases in γ-lamellar fraction and colony size observed between 1 and 2 °C/s.
4. At 1350 °C, the system also exhibits strong sensitivity to minor temperature fluctuations, highlighting the importance of precise thermal control.
5. It remains to be confirmed whether the observed changes are primarily driven by cooling rate or duration within the phase fields.
6. FAST processing demonstrates strong potential for producing optimal pre-forging microstructures in peritectic

solidifying titanium aluminides. A dwell temperature around 1350 °C provides the most favourable balance, promoting γ-lamellar structure formation without inducing excessive grain growth, making it ideal for forging applications. Further studies looking at varying the dwell temperatures at this temperature will aim to reduce the γ-lamellar colony size while maintaining a fully γ-lamellar volume fraction.

Acknowledgments

Firstly, we acknowledge the financial support of the project by Boeing UK and thank Mykola Kulakov and David Milliken for their continued guidance. The research was funded by Science Foundation Ireland (18/EPSRC-CDT/3584) and the Engineering and Physical Sciences Research Council UK (EP/S022635/1) through the Advanced Metallic Systems Centre for Doctoral Training. We also acknowledge EPSRC for the field-assisted sintering technology (FCT HP D25, FCT HP D250) capabilities as part of the Henry Royce Institute (grants EP/R00661X/1, EP/P02470X/1, EP/S019367/1 and EP/X52850X/1). Finally, we acknowledge FAST/SPS technical support from Nigel Adams and the Sheffield Titanium Alloy Research team for their advice and technical support in this research.

Funding

This study was supported by Science Foundation Ireland (18/EPSRC-CDT/3584), The Engineering and Physical Sciences Research Council UK (EP/S022635/1), and Engineering and Physical Sciences Research Council (EP/R00661X/1, EP/P02470X/1, EP/S019367/1 and EP/X52850X/1).

Conflicts of Interest

The authors declare no conflicts of interest.

Data Availability Statement

The data that support the findings of this study are available from Jack Krohn upon request.

References

1. G.-R. Li, J.-Z. Zhou, H.-M. Wang, et al., "Progress in Performance Optimization of Ti-al Alloys for Aviation via Physical Field Application and Alloying," *Journal of Materials Engineering and Performance* 2026 (2026): 1–22.

2. F. Appel, J. D. H. Paul, and M. Oehring, Gamma Titanium Aluminide Alloys (Wiley-VCH, 2011).

3. G. Lütjeringand J. Williams, Titanium Based Intermetallics (Springer, 1985), 289–325.

4. S.-K. Rittinghausand J. Zielinski, "Influence of Process Conditions on the Local Solidification and Microstructure during Laser Metal Deposition of an Intermetallic Tial Alloy (ge4822)," *Metallurgical and Materials Transactions A* 52 (2021): 1106–1116.

5. E. S. Bumps, H. D. Kessler, and M. Hansen, "Titanium-Aluminum System," *JOM* 4 (1952): 609–614.

6. E. L. Hall, and S.-C. Huang, "Microstructures of Rapidly-Solidified Binary Tial Alloys," *Acta Metallurgica et Materialia* 38 (1990): 539–549.

7. J. L. Murray, "Calculation of the Titanium-Aluminum Phase Diagram," *Metallurgical Transactions A* 19 (1988): 243–247.

8. E. S. C. Chinand R. R. Biederman, The Titanium-Aluminum Phase Diagram. a Review of the near Ti-50 at.al Phase Fields (Worcester Polytechnic Institute, 1992).

9. H. R. Ogden, D. J. Maykuth, W. L. Finlay, and R. I. Jaffee, "Constitution of Titanium-Aluminum Alloys," *JOM* 3 (1951): 1150–1155.

10. C. McCullough, J. J. Valencia, C. G. Levi, and R. Mehrabian, "Phase Equilibria and Solidification in Ti-al Alloys," *Acta Metallurgica* 37 (1989): 1321–1336.

11. J. C. Schuster, and M. Palm, "Reassessment of the Binary Aluminum-Titanium Phase Diagram," *Journal of Phase Equilibria and Diffusion* 27 (2006): 255–277.

12. Y. Yang, H.-L. Chen, Q. Chen, et al., "Development of Calphad Database for Both Ti- and Tial-Based Alloys," *MATEC Web of Conferences* 321 (2020): 12011.

13. Thermo-Calc Software AB, Thermo-Calc Software (TCS Ti/TiAl-based Alloys Database TCTI6, 2025.

14. R. M. Imayev, V. M. Imayev, M. Oehring, and F. Appel, "Alloy Design Concepts for Refined Gamma Titanium Aluminide Based Alloys," *Intermetallics* 15 (2007): 451–460.

15. S. Kremmer, H. F. Chladil, H. Clemens, A. Otto, and V. Güther, Near Conventional Forging of Titanium Aluminides (Japan institute of metals, 2007).

16. V. Seetharamanand S. L. Semiatin, "Effect of the Lamellar Grain Size on Plastic Flow Behavior and Microstructure Evolution during Hot Working of a Gamma Titanium Aluminide Alloy," *Metallurgical and Materials Transactions A: Physical Metallurgy and Materials Science* 33 (2002): 3817–3830.

17. B. W. Zhao, L. I. G.R., Y. X. Guo, Y. Liu, H. M. Wang, and Z. J. Ji, "Mechanism of Magnetic Fragmentation Effect on Mechanical Properties of Tial Alloy Modified by Combined Magnetic-Thermal Treatment," *Materials Today Communications* 43, no. 111678 (2025): 2.

18. H. M. Wang, K. K. Li, G. R. Li, B. W. Zhao, X. M. Zhao, and Z. J. Ji, "Significantly Enhanced Strength-Ductility Synergy in Ti-al-Based Alloy at 800 °C Subjected to Pulsed Magnetic Field Treatment (pmt)," *Journal of Alloys and Compounds* 182041 (1036): 7.

19. K. K. Li, X. M. Zhao, J. Z. Zhou, H. M. Wang, G. R. Li, and X. F. Ding, "Effect of Combined Pulsed Magnetic Treatment and Low-Temperature Annealing on the Microstructure and Mechanical Properties of as-Cast Ti-al-x(cr, v, Zr) Alloy," *Journal of Alloys and Compounds* 1051 (2026): 186001.

20. N. S. Weston, F. Derguti, A. Tudball, and M. Jackson, "Spark Plasma Sintering of Commercial and Development Titanium Alloy Powders," *Journal of Materials Science* 50 (2015): 4860–4878.

21. N. S. Weston, B. Thomas, and M. Jackson, "Processing Metal Powders via Field Assisted Sintering Technology (fast): A Critical Review," *Materials Science and Technology* 35 (2019): 1306–1328.

22. A. A. Abdelhakim, "Spark Plasma Sintering of Titanium Aluminide Intermetallics and its Composites," (PhD thesis, Oklahoma State University, 2005).

23. T. Voisin, J.-P. Monchoux, M. Perrut, and A. Couret, "Obtaining of a Fine Near-Lamellar Microstructure in Tial Alloys by Spark Plasma Sintering," *Intermetallics* 71 (2016): 88–97.

24. B.-A. Behrens, K. Brunotte, J. Peddinghaus, and A. Heymann, "Influence of Dwell Time and Pressure on Sps Process with Titanium Aluminides," *Metals* 12 (2022): 83.

25. X. Liu, Q. Lin, W. Zhang, C. Van Horne, and L. Cha, "Microstructure Design and Its Effect on Mechanical Properties in Gamma Titanium Aluminides," *Metals* 11 (2021): 1644.

26. Z. Li, L. Luo, Y. Su, et al., In-Situ Study on γPhase Transformation Behaviour of γ-Tial Alloys at Different Cooling Rates, *Progress in Natural Science: Materials International* 32, no. 3 (2022): 345–357.

27. P. Au, "*A Heat Treatment Procedure to Produce Fine Grained Lamellar Microstructures in P/M Titanium Aluminide Alloy*," (PhD thesis, Ottawa-Carleton Institute, 1997), 3.

28. C. A. Schneider, W. S. Rasband, and K. W. Eliceiri, "NIH Image to ImageJ: 25 Years of Image Analysis," *Nature Methods* 9, no. 7 (2012): 671–675.

29. ASTM E384, Standard Test Method for Microindentation Hardness of Materials (ASTM International, 2022).

30. COMSOL AB, COMSOL Multiphysics (Version 5.4) [Computer software] (COMSOL AB, 2018).

31. M. Xiao, L. Tang, X. Zhang, I. Y. F. Lun, and Y. Yuan, "A Review on Recent Development of Cooling Technologies for Concentrated Photovoltaics (cpv) Systems," *Energies* 11 (2018): 12.

32. C. Manière, A. Pavia, L. Durand, G. Chevallier, K. Afanga, and C. Estournès, "Finite-Element Modeling of the Electro-Thermal Contacts in the Spark Plasma Sintering Process," *Journal of the European Ceramic Society* 36 (2016): 741–748.

33. I. Egry, R. Brooks, D. Holland-Moritz, et al., "Thermophysical Properties of γ-Titanium Aluminide: The European Impress Project," *International Journal of Thermophysics* 28 (2007): 1026–1036.

34. J. Pepper, O. L. Blanch, B. Thomas, and M. Jackson, "Channelling Electric Current during the Field-Assisted Sintering Technique (fast) to Control Microstructural Evolution in Ti-6al-4v," *Journal of Materials Science* 58 (2023): 14514–14532.

35. R Core Team, R: A Language and Environment for Statistical Computing [Computer software] (R Foundation for Statistical Computing, 2025).

36. S. E. Hoosain, S. Pityana, C. S. Freemantle, and M. Tlotleng, "Heat Treatment of In Situ Laser-Fabricated Titanium Aluminide," *Metals* 8 (2018): 9.

37. ASTM E2371, Standard Test Method for Analysis of Titanium and Titanium Alloys by Direct Current Plasma and Inductively Coupled Plasma Atomic Emission Spectrometry (ASTM International, 2021).

38. ASTM E1409, Standard Test Method for Determination of Oxygen and Nitrogen in Titanium and Titanium Alloys by Inert Gas Fusion (ASTM International, 2021).

39. ASTM E1915, Standard Test Methods for Analysis of Metal Bearing Ores and Related Materials for Carbon, Sulfur, and Acid-Base Characteristics (ASTM International, 2020).

40. H. J. Yang, Y. T. Pei, J. C. Rao, and J. T. M. De Hosson, "Self-Healing Performance of Ti_2Alc Ceramic," *Journal of Materials Chemistry* 22 (2012): 8304–8313.

41. S. Hashimoto, M. Takeuchi, K. Inoue, et al., "Pressureless Sintering and Mechanical Properties of Titanium Aluminum Carbide," *Materials Letters* 62 (2008): 1480–1483.